SCIENCE CHINA
Information Sciences

• RESEARCH PAPER •

May 2025, Vol. 68, Iss. 5, 150306:1–150306:18
https://doi.org/10.1007/s11432-024-4373-7

Special Topic: Integrated Sensing and Communications Techniques for 6G

OFDM-structure based waveform designs for integrated sensing and communication

Jiaqi LIU[1], Ping YANG[1*], Ke JIANG[1], Jiarong ZHAO[1], Wei XIANG[2], Jianping WEI[3], Ruixiang DUAN[3], Saviour ZAMMIT[4] & Tony Q. S. QUEK[5]

[1]*National Key Laboratory of Wireless Communications, University of Electronic Science and Technology of China, Chengdu 611731, China*
[2]*School of Computing Engineering and Mathematical Sciences, La Trobe University, Melbourne VIC 3086, Australia*
[3]*Meituan Academy of Robotics, Shenzhen 518071, China*
[4]*Department of Communications and Computer Engineering, University of Malta, Msida MSD 2080, Malta*
[5]*Information Systems Technology and Design Pillar, Singapore University of Technology and Design, Singapore 487372, Singapore*

Received 20 November 2024/Revised 19 February 2025/Accepted 2 April 2025/Published online 24 April 2025

Abstract The future sixth-generation (6G) paradigm aims to seamlessly integrate communication and environmental sensing capabilities into a single radio signal, promising improved efficiency and cost-effectiveness through simultaneous data communications and environmental perception. At the core of this evolution, orthogonal frequency division multiplexing (OFDM) and its advanced waveforms emerge as pivotal for integrated sensing and communications (ISAC). This study introduces a concise and unified ISAC waveform design framework based on orthogonal multicarriers. This framework supports versatile applications of OFDM and its derivative waveforms within a generalized ISAC system, marking a significant leap in integrating communication and sensing capabilities. A distinguishing feature of this framework is its adaptability, allowing users to intelligently select modulation strategies based on their specific environmental needs. This adaptability optimizes performance across diverse scenarios. Central to our innovations is the proposal of discrete Fourier transform-spread OFDM with index modulation (DFT-S-OFDM-IM). This framework is paired with newly proposed signal processing methods for single-input single-output and multiple-input multiple-output (MIMO) systems. Extensive evaluations highlight DFT-S-OFDM-IM's superiority, including dramatically reduced peak-to-average power ratios (PAPRs), competitive communication performance, and exceptional sensing capabilities, striking an elegant balance between communication capacity and environmental sensing precision.

Keywords DFT-S-OFDM-IM, index modulation, integrated sensing and communication, OFDM

Citation Liu J Q, Yang P, Jiang K, et al. OFDM-structure based waveform designs for integrated sensing and communication. Sci China Inf Sci, 2025, 68(5): 150306, https://doi.org/10.1007/s11432-024-4373-7

1 Introduction

As we move toward sixth-generation (6G) technology, an emerging trend is the convergence of wireless communication and sensing functionalities. This integration becomes particularly pronounced as wireless communications extend into higher frequency bands, such as millimeter waves and terahertz bands. The shared use of devices or components for integrated communications and sensing stands out as a critical requirement for 6G systems [1–3]. These upcoming 6G wireless communication networks are poised to integrate communication and sensing, heralding a transformative era where devices are sensor-equipped, interconnected, and intelligent [4]. The envisioned system will enable simultaneous message transmission and environmental sensing through radio signals, promising enhanced spectral efficiency and reduced hardware costs [5, 6].

Orthogonal frequency division multiplexing (OFDM) signals, known for their high spectral efficiency and resistance to intersymbol interference, are widely used in wireless communication systems. In recent years, the development of communication-sensing integration technology has heightened interest in using OFDM waveforms as dual-function signals. In [7], Levanon pioneered the proposal of utilizing OFDM waveforms for target detection. The work in [8] explored the simultaneous use of OFDM waveforms for

* Corresponding author (email: yang.ping@uestc.edu.cn)

target detection and information transmission. For instance, researchers introduced novel radar signal processing methods leveraging OFDM, allowing the manipulation of modulation symbols directly rather than baseband signals. This approach overcomes drawbacks associated with traditional correlation-based processing methods. In [9], the authors proposed a novel radar system based on OFDM to enhance the multi-user capability and physical layer security. OFDM signal integration with linear frequency modulated carriers introduced in [10] demonstrated the ability to combine the distance resolution of linear frequency modulation with the maximum measurable velocity achievable with OFDM modulation. In [11], a joint sequence optimization approach for dual-function OFDM waveforms was proposed, simultaneously enhancing radar target detection probability, communication synchronization accuracy, and information transmission efficiency. Similarly, waveform designs based on sequence optimization, such as those utilizing zero correlation zone (ZCZ) and zero odd-correlation zone (ZOCZ) sequences [12], have shown promise. These channels simultaneously support channel estimation and radar sensing within integrated sensing and communication (ISAC) systems.

In summary, shared waveform technology based on OFDM plays a crucial role in integrating radar and communication systems [7–11]. In the field of communications, OFDM is a core technology in modern mobile communications and is extensively applied across various communication standards. On the radar front, OFDM proves instrumental in expanding signal bandwidth and enhancing radar resolution. However, despite its widespread adoption, OFDM signals face inherent limitations, including a high peak-to-average power ratio (PAPR) and diminished resilience against sudden channel impairments [13]. Recently, novel waveform technologies such as orthogonal time-frequency space modulation (OTFS) and affine frequency division multiplexing (AFDM) [14, 15] have been explored for 6G. Nonetheless, OFDM structures continue to be a key focus in research and remain highly relevant.

Discrete Fourier transform-spread OFDM (DFT-S-OFDM) [16] is an evolved version of OFDM. Unlike traditional OFDM, DFT-S-OFDM utilizes a DFT to map the signal into the frequency domain before modulating it back to the time domain through an inverse DFT (IDFT). The counteracting effect between DFT and IDFT reduces the PAPR of the transmitted signal, minimizing distortion risks. Additionally, DFT-S-OFDM allocates continuous data to multiple subcarriers using DFT, effectively enhancing resilience to multipath effects and reducing the bit error rate (BER) compared to conventional OFDM. Recent studies have explored the integration of DFT-S-OFDM in radar communication systems. For example, in [17], the authors investigated its use in medium-range single-input single-output (SISO) and multiple-input multiple-output (MIMO) radar systems. These studies demonstrate that DFT-S-OFDM retains radar characteristics similar to OFDM while considerably reducing PAPR. However, most of this research has been preliminary, focusing on foundational aspects without proposing uniform waveform designs or optimization frameworks to address multifunctional requirements.

Index modulation (IM) schemes have recently emerged as a focal area of research, showing great promise for advancing 6G modulation techniques [18]. These schemes rely on conveying information through specific unit indices, such as transmit antennas, subcarriers, and time intervals [19–21]. By incorporating these indices into transmitted or received signals, IM methods eliminate the need for additional energy to encode index information. These schemes have led to notable improvements in both spectral and energy efficiency [22, 23]. Ref. [24] proposed an innovative methodology known as circularly-shifted chirps with index modulation (CSC-IM), specifically tailored for ISAC systems. This pioneering approach incorporates CSCs to encode information bits while employing phase-shift keying (PSK) symbols. The integration of IM with wideband CSCs empowers the receiver to sufficiently exploit frequency selectivity in fading channels. Furthermore, the inherent constant-envelope characteristic of CSCs helps maintain controlled peak-to-mean envelope power ratios (PMEPRs). Ref. [25] further exploited the benefits of IM in ISAC systems, where spatial- and frequency-domain index modulation techniques are used to explore additional dimensions and enhance resource utilization efficiency.

Compared to index modulation, DFT-S-OFDM offers a promising approach for further reducing PAPR owing to its single-carrier waveform characteristics [25–28]. However, current research has predominantly focused on DFT spread without thoroughly exploring its potential or integration with IM, which remains scarcely addressed in existing literature. To bridge this research gap, we propose a novel DFT-S-OFDM with IM (DFT-S-OFDM-IM) waveform, which integrates DFT-spread and IM into a unified framework. This synergy allows us to fully exploit the strengths of each technique: DFT-spread reduces PAPR, while IM strikes a balance between BER performance and spectral efficiency.

Specifically, this paper proposes a general framework for ISAC communications based on OFDM and its evolved waveforms alongside a novel dual-function waveform, namely DFT-S-OFDM-IM. Our novel

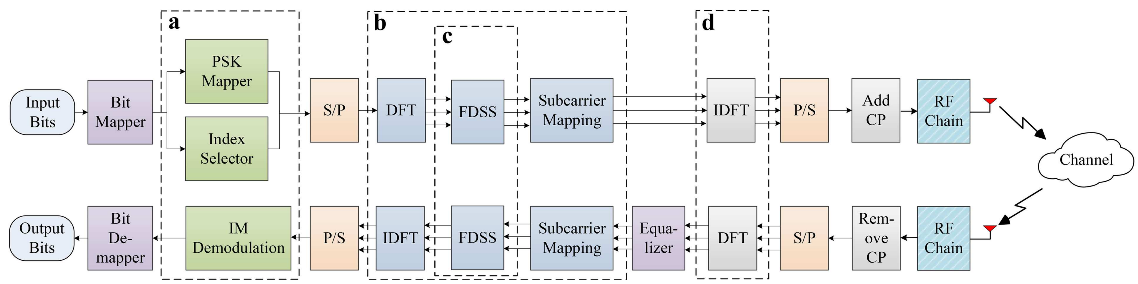

Figure 1 (Color online) Unified transmission chain framework (communication systems).

contributions can be summarized as follows.

(1) We propose a novel waveform design, termed DFT-S-OFDM-IM, and provide a comprehensive presentation of OFDM variants, encompassing OFDM-IM, CSC-IM, and DFT-S-OFDM. Our unique contribution lies in summarizing these waveform variants within a concise and unified framework. This framework covers the numerical criteria and distinctive characteristics of each waveform.

(2) Utilizing the proposed framework, we propose specialized signal processing methods for both communication and radar receivers in ISAC systems, with support for SISO and MIMO setups. Our design incorporates two distinct types of index modulation techniques, namely non-packet index modulation (NPIM) and packet index modulation (PIM). In this paper, we design different communication and sensing signal processing methods for different indexing scenarios.

(3) We conduct comprehensive performance comparisons of the proposed waveform against the aforementioned orthogonal multicarrier-based waveforms in ISAC systems. Key performance metrics considered include the PAPR, BER, and target detection hit rate. Our simulation results highlight DFT-S-OFDM-IM's superiority, showcasing significant advantages in PAPR reduction, BER performance, and exceptional sensing capabilities. The findings reveal that the proposed waveform strikes a promising balance between communication efficiency and sensing precision.

The remainder of this paper is organized as follows. Section 2 introduces the basic principles of OFDM and its advanced waveforms. Section 3 outlines the signal processing procedures for the integrated SISO model using DFT-S-OFDM-IM. Section 4 introduces the parameter estimation methods, while Section 5 covers the signal processing procedures for the integrated MIMO model. Section 6 presents a thorough simulation analysis of the communication and sensing performance of different waveform designs. Finally, Section 7 concludes the paper.

2 Evolutionary waveforms of OFDM

In order to facilitate the demonstration and illustration of the relationship between OFDM and its evolutionary waveforms, we propose a unified transmission chain framework. As shown in Figure 1, we suggest marking specific structures as four sub-blocks labeled as '**a**', '**b**', '**c**' and '**d**'. We provide a list of different modulation schemes that can be obtained by enabling or disabling these sub-blocks, covering a wide range of communication technologies. It is noted that this is a concise and unified ISAC waveform design framework based on orthogonal multicarriers, which enables versatile applications of all OFDM and its derivative waveforms under a generalized ISAC system. From these four sub-blocks, we can define a variety of OFDM-based modulation schemes. This paper focuses primarily on the following five schemes.

- $\mathbf{d}$: conventional OFDM.
- $\mathbf{a} + \mathbf{d}$: OFDM-IM.
- $\mathbf{b} - \mathbf{c} + \mathbf{d}$: DFT-S-OFDM.
- $\mathbf{a} + \mathbf{b} + \mathbf{d}$: CSC-IM.
- $\mathbf{a} + \mathbf{b} - \mathbf{c} + \mathbf{d}$: DFT-S-OFDM-IM.

2.1 DFT-S-OFDM

In DFT-S-OFDM, the transmitted signal undergoes a DFT to spread the spectrum in the frequency domain. At the receiver, an IDFT is performed to recover the original data. This process is associated with the sub-block '**b**'−'**c**'. Due to the inherent cancelation property between DFT and IDFT operations, the DFT-S-OFDM signal can be equivalently considered as a single-carrier signal.

DFT-S-OFDM highlights the following advantages.

(1) Low PAPR. DFT-S-OFDM combines DFT and IDFT operations, resulting in a signal with reduced PAPR. This lowers the probability of peak values occurring.

(2) Strong multipath resistance. The DFT precoding offers robust resistance to multipath fading in the time domain, mitigating inter-symbol interference (ISI) and frequency-selective fading effects.

2.2 OFDM-IM

In traditional OFDM systems, bit information is typically modulated using classic PSK/QAM methods, and then mapped to be constellation points. However, OFDM-IM introduces a novel approach. It divides input bits into two groups. The first group is dedicated to determining the indices of the OFDM subcarriers activated for transmission, while the second group is used for conveying information through classic PSK/QAM on these active subcarriers. At the receiver, the activated subcarrier is detected, allowing the corresponding bits to be decoded. This functionality is achieved through the utilization of sub-block '**a**'.

Assuming that N_G subcarriers in each group decide to activate one for symbol transmission based on the index bit, the transmit vector is denoted by

$$\boldsymbol{u} = \left(\underbrace{0, \ldots, 0, s_1, 0, \ldots, 0}_{N_G}, 0, \ldots, s_2, \ldots, 0, \ldots, s_G, \ldots, 0\right). \tag{1}$$

Based on (1), the corresponding baseband time-domain signal can be given by

$$x\left(t\right) = \sum_{n=1}^{N} u\left(n\right) \mathrm{e}^{\mathrm{j}2\pi f_n t}, \tag{2}$$

where $u\left(n\right)$ is the n-th element of $\boldsymbol{u}$, N is the number of the total subcarriers and f_n is the frequency used for the n-th carrier. Compared to traditional OFDM, OFDM-IM offers several compelling advantages.

(1) Improved BER performance. By incorporating a subcarrier index to carry part of the bit information, OFDM-IM extends the modulation dimension and is capable of enhancing the transmission reliability.

(2) Flexible subcarrier activation. The number of activated subcarriers in OFDM-IM can be adjusted to match the desired transmission rate, providing adaptable system configurations for different applications. It is worth noting that OFDM can be viewed as a special case of OFDM-IM.

(3) Reduced PAPR and interference. Selectively activating subcarriers in OFDM-IM lowers the peak power and inter-carrier interference, resulting in improved power efficiency and signal quality.

2.3 CSC-IM

CSC-IM is a novel waveform for ISAC systems. Initially, Şahin et al. [29] demonstrated that DFT-S-OFDM can generate modulatable CSC signals through well-designed frequency-domain spectral shaping (FDSS) filters. However, the combination of CSC and ISAC was not well addressed in [29]. In 2022, Şahin et al. [24] proposed a CSC-IM technique, which enables simultaneous radar detection and information transmission with low PAPR. This work provides evidence for the effectiveness of CSC-IM signals in ISAC scenarios.

The baseband CSC signal after discrete sampling [24] can be expressed as

$$x(n) = \sum_{k=L_d}^{L_u} c_k \sum_{m=0}^{M-1} d(m) \mathrm{e}^{-\frac{\mathrm{j}2\pi km}{M}} \mathrm{e}^{\frac{\mathrm{j}2\pi kn}{N}}, \quad n = 0, 1, \ldots, N-1, \tag{3}$$

where $L_d < 0$, $L_u > 0$, and both are integers, c_k is the Fourier coefficient, $N \geqslant L_u - L_d + 1 = M$, and $d(m)$, $m = 0, 1, \ldots, M-1$ represent constellation points. The CSC can be regarded as a special process of DFT-S-OFDM. The detailed steps are as follows.

Step 1. Perform an M-point DFT on the data symbols $d(m)$, $m = 0, 1, \ldots, M-1$ (sub-block '**b**').

Step 2. Multiply each element of the DFT-transformed sequence with the corresponding Fourier coefficient c_k, i.e., FDSS (sub-block '**c**').

Step 3. Similar to the spreading process in DFT-S-OFDM, add zero symbols to the output of the FDSS to fill the remaining $N-(L_u-L_d+1)$ subcarriers.

Step 4. Compute the N-point IDFT on the padded sequence (sub-block '**d**').

The specific steps of CSC signal processing reveal its remarkable similarity to DFT-S-OFDM. The key distinction lies in the inclusion of the coefficients c_k for frequency-domain shaping. By selecting the appropriate expression of c_k, a diverse range of chirp signals can be generated, such as sine waves, linear waves, as well as triangular waves. For instance, the k-th Fourier coefficient of a linear chirp can be calculated as [26]

$$c_k=\gamma_k\left\{C(\alpha_k)+C(\beta_k)+\mathrm{j}S(\alpha_k)+\mathrm{j}S(\beta_k)\right\}, \tag{4}$$

where $C(\cdot)$ and $S(\cdot)$ represent the Fresnel integrals with cosine and sine functions, respectively. Moreover, we have $\gamma_k=\sqrt{\frac{\pi}{D}}\mathrm{e}^{-\frac{\mathrm{j}2(\pi k)^2}{D}-\mathrm{j}\pi k}$, $\alpha_k=\frac{D/2+2\pi k}{\sqrt{\pi D}}$ and $\beta_k=\frac{D/2-2\pi k}{\sqrt{\pi D}}$, where D is a positive real-valued number and satisfies $D\leqslant M$. Let Δf be the subcarrier spacing, the total bandwidth of the system is $D\Delta f$.

2.4 DFT-S-OFDM-IM

CSC-IM incorporates information onto selected portions of the chirp signal while assigning zeros to the remaining positions to preserve the integrity of the cyclic chirp structure. Note that if the modulation information is too dense in the time domain, it will significantly reduce the performance of the system. To address this issue, this paper proposes a novel DFT-S-OFDM-IM waveform, which combines index modulation with DFT-S-OFDM. Unlike traditional OFDM-IM, DFT-S-OFDM-IM performs indexing in the time domain rather than on frequency-domain subcarriers. Additionally, DFT-S-OFDM-IM differs from CSC-IM as it does not directly modulate the chirp signal but selects different sub-time slots for modulation (compared to OFDM-IM, DFT-S-OFDM-IM is a time-domain based index modulation scheme). By using index values, it determines which sub-time slots transmit data and which sub-time slots remain idle, achieving the goal of information transmission.

Specifically, as shown in Figure 1, for DFT-S-OFDM-IM, the transmit bits undergo slot-wise index modulation (sub-block '**a**'), followed by a DFT in the frequency domain (sub-block '**b**'–'**c**'), and then subcarrier mapping and an IDFT (sub-block '**d**'), among other processes. DFT-S-OFDM-IM activates one time slot per group for symbol transmission, and its transmit vector is denoted by

$$\boldsymbol{u}=\left(\underbrace{0,\ldots,0,s_1,0,\ldots,0}_{N_G},\ldots,0,\ldots,s_G,\ldots,0\right). \tag{5}$$

The signal $u(m)$ is then subjected to an M-point DFT to obtain the frequency-domain signal $X(k)$ as follows:

$$X(k)=\sum_{m=0}^{M-1}u(m)\mathrm{e}^{-\frac{\mathrm{j}2\pi km}{M}},\quad k=0,1,\ldots,M-1. \tag{6}$$

The next step is subcarrier mapping, where $X(k)$ is assigned to N subcarriers, with $S=\frac{N}{M}$ being a positive integer known as the spreading factor. During the early stages of LTE standardization, there was consideration for a distributed subcarrier mapping scheme. However, due to the limitations in channel estimation accuracy with the distributed mapping approach using DFT-S-OFDM, LTE adopted a centralized subcarrier allocation scheme. As a result, the frequency domain signal after centralized subcarrier allocation is

$$\boldsymbol{X}=\left[X(0),X(1),\ldots,X\left(\frac{M}{2}-1\right),0,\ldots,0,X\left(\frac{M}{2}+1\right),\ldots,X(M-1)\right]. \tag{7}$$

The time-domain signal of DFT-S-OFDM-IM $x(n)$ is obtained by performing the IDFT on the spread signal, i.e.,

$$x(n)=\sum_{k=0}^{MS-1}\sum_{m=0}^{M-1}u(m)\mathrm{e}^{-\frac{\mathrm{j}2\pi km}{M}}\mathrm{e}^{\frac{\mathrm{j}2\pi kn}{N}},\quad n=0,1,\ldots,N-1. \tag{8}$$

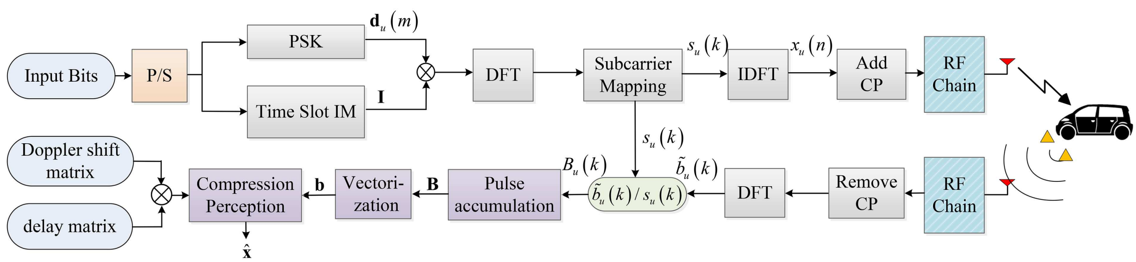

Figure 2 (Color online) Block diagram of radar signal processing for the DFT-S-OFDM-IM waveform in a SISO system.

Afterward, the signal undergoes serial-to-parallel conversion and cyclic prefix (CP) insertion. Then, it is transmitted through the RF chain. At the receiver, the signal is processed through the reverse process of the transmitter as shown in Figure 1.

The distinguishing feature of the DFT-S-OFDM-IM system compared to CSC-IM is that it eliminates the need for spectrum shaping, i.e., there is no subblock '**c**', thus simplifying the signal processing. It effectively combines the advantages of DFT-S-OFDM and OFDM-IM, offering more advantages in PAPR and BER, as will be shown in Section 6.

3 System model

We consider an ISAC system based on the aforementioned orthogonal waveforms, where its base station (BS) transmits communication signals to the users and simultaneously receives the echoes reflected from the surrounding targets. In the SISO scenarios, the BS is equipped with a single dual-function transmit antenna and a single radar receive antenna, and the user side is equipped with a single communication receiving antenna. In this section, as shown in Figure 2, we focus on the DFT-S-OFDM-IM as an example to illustrate the basic model and main units of the system.

3.1 Communications signal model

To enable seamless index modulation in ISAC waveforms, we propose a unified framework that categorizes index modulation into two distinct types: NPIM and PIM. The former is better suited for scenarios where a smaller number of subcarriers or time slots are needed, while the latter is more appropriate for situations where a larger number of subcarriers or time slots are required. This categorization enables a more systematic and efficient approach to implementing index modulation in ISAC waveforms.

Specifically, the NPIM model is well-suited for scenarios where channel conditions are unfavorable, while the PIM model is more suitable for applications that require higher data rates and improved robustness against channel impairments. By categorizing index modulation in this manner, we can better tailor its use to the specific requirements of each application, thereby enhancing the overall performance and flexibility of ISAC waveforms.

In the NPIM model, K time slots out of M are selected for activation, i.e., $K \ll M$. The total number of bits that can be transmitted by sending J-order modulation scheme on K time slots is

$$N_{np} = \left\lfloor \log_2(C_M^K) \right\rfloor + \left\lfloor K \log_2(J) \right\rfloor . \tag{9}$$

Set $\boldsymbol{I} = (i_0, i_1, \ldots, i_{K-1})$, where i_k denotes the position of the time slot corresponding to the k-th index. Consider the modulation method as PSK, and $\boldsymbol{J} = (j_0, j_1, \ldots, j_{K-1})$ denotes the phase vector modulated by PSK, then the achieved modulation symbol on the i_k-th time slot is $d(i_k) = \exp(\mathrm{j}2\pi j_k/J)$.

Denote by S_k the integer interval between two adjacent indices, where $k \in \{0, \ldots, K-1\}$. Introduce constraints on it as follows:

$$S_k \triangleq \begin{cases} i_k - i_{k-1} - 1, & 0 \leqslant k < K-2, \\ M - 1 - i_{K-1} + i_0, & k = K-1. \end{cases} \tag{10}$$

The objective of controlling the time slot interval can be achieved by setting $S_k \geqslant \Delta, \Delta \in \mathbb{N}^*$. In NPIM, this process is to achieve the setting of the minimum sub-slot interval, which can ensure the separation of transmitted information and reduce interference between signals.

The benefit of the NPIM model is that the average spacing between active time slots is large and there is less interference between signals, resulting in a lower BER of the transmitted signal. For CSC-IM waveforms, a lower index number also means less impact on the waveform, thus not destroying its cyclic chirp structure.

The PIM model usually requires grouping of time slots, and for each group a fixed number of indices are selected for activation. The M time slots are divided into G groups, and each group of M_g time slots constitutes a sub-block, i.e., $M = GM_g$. For each sub-block the same IM process is performed. The input information bits are divided into two parts: the first part is the number of subcarriers or time slots selected for activation; the second part is mapped to J-ray PSK/QAM constellation to determine the data symbols of the active subcarriers or time slots. It is worth noting that except for the activated subcarriers, the unselected subcarriers or time slots keep silent and does not carry information. Denoting by M_s and J the number of selected subcarriers or time slots per group and the modulation order, respectively, the total number of transmittable bits is

$$N_p = G \left\lfloor \log_2 (C_{M_g}^{M_s}) \right\rfloor + G \left\lfloor M_s \log_2 J \right\rfloor . \tag{11}$$

As shown in Figure 2, the implementation of DFT-S-OFDM-IM requires the removal of the CP at the communication receiver and the application of an M-point DFT to the received signal. Considering a spreading factor of 1, the resulting signal can be mathematically expressed as

$$b(k) = \lambda_k \sum_{m=0}^{M-1} d(m) \mathrm{e}^{-\mathrm{j}2\pi k \frac{m}{M}} + w_k, \quad k = 0, \ldots, M-1, \tag{12}$$

where λ_k denotes the frequency-domain response between the transmit and receive antennas at the k-th time slot, and w_k is a zero-mean additive white Gaussian noise (AWGN) with variance σ_k^2.

We perform minimum mean square error (MMSE) based frequency-domain equalization of the remove the effects of the channels and then use an N-point IDFT to obtain the estimation of the modulation symbols on the subcarriers, given by

$$\tilde{d}(m) = \sum_{k=0}^{M-1} \frac{\lambda_k^*}{|\lambda_k|^2 + \sigma_k^2} b(k) \mathrm{e}^{\mathrm{j}2\pi k \frac{m}{M}}, \quad m = 0, \ldots, M-1. \tag{13}$$

Then, based on (13), we can carry out the demodulation of IM to obtain the transmit bits, which will be detailed in Subsection 3.3.

3.2 Radar signal model

In this subsection, we consider ISAC BS employing DFT-S-OFDM-IM frames with N_{syms} DFT-S-OFDM-IM symbols to sense its surrounding targets and derive a DFT-S-OFDM-IM based signal model of target echoes.

To enhance the conciseness of the model, the following assumptions are made regarding the received signal:

(1) The transmitted signal is considered a narrowband signal, and the target is assumed to be a point target;

(2) Within each coherent processing interval (CPI), the target is assumed to reside in the same range cell or the range migration has been compensated;

(3) The target's Doppler frequency shift falls within the Doppler ambiguity limit, and the phase variation caused by the Doppler frequency shift can be approximated as negligible within the pulse duration.

It is noted that these assumptions may not be fully applicable in complex scenarios, but they provide sufficient accuracy and practicality in most cases. Hence, many ISAC related studies are conducted under these assumptions, such as [24, 25]. Under the aforementioned assumptions, we establish a sensing model for a single point target. The radar channel is considered a Gaussian channel. Denote by R the distance to the target, and V represents the radial velocity. Note that V determines by the time delay of $\tau = 2R/c$ and the target's Doppler frequency shift $f_d = 2f_c V/c$, where c denotes the speed of light.

When the transmitted signal is the DFT-S-OFDM-IM shared signal, the complex-valued envelope of the echo from the target, after the effective removal of the CP in the received signal, can be expressed as

$$y(t) = \alpha x(t-\tau)\mathrm{e}^{\mathrm{j}2\pi f_d t} + \omega\left(t\right), \tag{14}$$

where α is the reflection coefficient of the target which is determined by the reflective area of the target and the signal attenuation, τ is the time delay due to the distance between the target and the observation point, f_d is the Doppler shift due to the radial motion of the target, and $\omega\left(t\right)$ denotes additive Gaussian white noise with variance σ^2.

Sampling $y(t)$ with sampling rate $f_s = B$ and sampling interval $T_s = 1/N\Delta f$, the discrete signal of a single pulse can be obtained as

$$y(k) = \eta_k \sum_{k=0}^{N-1}\sum_{m=0}^{M-1} d(m)\mathrm{e}^{-\mathrm{j}2\pi k\frac{m}{M}}\mathrm{e}^{\mathrm{j}2\pi k\frac{n}{N}} + w_k, \tag{15}$$

where we have $k = 0, 1, \ldots, N-1$, $m = 0, 1, \ldots, M-1$, and $\eta_k = \alpha\mathrm{e}^{-\mathrm{j}2\pi k\Delta f\tau + \mathrm{j}2\pi f_d T_{\mathrm{PRI}}}$. Here, T_{PRI} is the pulse repetition interval (PRI), which will be detailed in (19).

3.3 Communications processing

In the context of IM, the receiver plays a crucial role in accurately detecting the indices of active subcarriers or time slots and their corresponding information symbols. The ML detector, known for its high accuracy, considers the exhaustive search among all legitimate index combinations and signal constellation points. If NPIM is used, the ML detection rule for the proposed DFT-S-OFDM-IM system is given as

$$\left\{\hat{\boldsymbol{I}}, \hat{\boldsymbol{J}}\right\} = \underset{i_{m_s}, j_{m_s}}{\arg\max}\left\{\sum_{m_s=0}^{M_s-1} \tilde{d}(i_{m_s})\mathrm{e}^{-\frac{\mathrm{j}2\pi j_{m_s}}{J}}\right\}, \tag{16}$$

where $\hat{\boldsymbol{I}}$ is the index vector of the active subcarriers and $\hat{\boldsymbol{J}}$ is the index vector of the PSK/QAM constellation points. If PIM is considered, the demodulation of the original signal can be achieved by performing the ML processing on each sub-block signal.

4 Parameter estimation methods

In this section, we focus on the design of radar sensing using DFT-S-OFDM-IM modulation. The radar signal processing model is illustrated in Figure 2. Remarkably, the methodology presented here holds potential for broader applicability, encompassing not only OFDM but also its various evolutionary waveforms.

In SISO systems, the objectives of radar signal processing are to estimate the distance, velocity and direction of multiple targets. The processing of echoes involves partitioning the signal into distinct range cells, with each cell corresponding to the distance and velocity of a specific target. By constructing an observation matrix, we can identify the range cell that exhibits the maximum amplitude response for the signal. The parameters associated with that particular range cell represent the estimated results for the targets.

Specifically, we take the detection of distance and velocity for a single target as an illustrative example. To avoid ISI, the condition that the time delay $\tau \leqslant T_{\mathrm{CP}}$ needs to be satisfied after removing the CP. Then, the maximum radar action distance and radar measurable distance accuracy are expressed as

$$R_{\max} = \frac{cT_{\mathrm{CP}}}{2}, \tag{17}$$

and

$$\Delta R = \frac{c}{2B}, \tag{18}$$

respectively, where B is the signal bandwidth, T_{CP} is the CP duration, and c represents the speed of light.

OFDM symbols are sent in pulses, and each pulse contains N_{syms} symbols, which are sent by combining an idle time. Here, we assume that the length of idle time is T_{off}. The purpose of adding the idle time is to improve the estimation performance of the signal for the Doppler shift, which can be used to adjust the speed measurement accuracy. The PRI is defined as

$$T_{\text{PRI}} = T_{\text{CP}} + N_{\text{syms}} T_s + T_{\text{off}}, \tag{19}$$

where the transmission time of each symbol is T_s. The maximum velocity can be expressed as

$$\nu_{\max} = \frac{c}{2 f_c T_{\text{PRI}}}. \tag{20}$$

In addition, due to the short duration of individual pulses, the amount of change in the Doppler shift caused by velocity is not obvious, we can improve the range accuracy by pulse accumulation, set the number of accumulated pulses as U, and the velocity measurement accuracy $\Delta\nu$ can be expressed as

$$\Delta\nu = \frac{c}{2 f_c U T_{\text{PRI}}}. \tag{21}$$

Based on (15), we first apply an N-point DFT to the u-th received signal, and the frequency-domain symbols are

$$\tilde{b}_u(k) = \eta_k \sum_{m=0}^{M-1} d(m) \mathrm{e}^{-\mathrm{j}2\pi k \frac{m}{M}} + \bar{w}_k, \tag{22}$$

where we have $k = 0, 1, \ldots, N-1$, $u = 0, 1, \ldots, U-1$, and $\bar{w}_k$ is the frequency-domain version of w_k.

Considering the data accumulated by U pulses together, we have

$$\begin{gathered}\tilde{b}(k) = \sum_{u=0}^{U-1} \eta_{u,k} \sum_{m=0}^{M-1} d_u(m) \mathrm{e}^{-\mathrm{j}2\pi k \frac{m}{M}} + w_{u,k}, \\ k = 0, \ldots, M-1,\ u = 0, 1, \ldots, U-1,\end{gathered} \tag{23}$$

where we have $\eta_{u,k} = \alpha \exp(-\mathrm{j}2\pi k \Delta f \tau + \mathrm{j}2\pi u f_d T_{\text{PRI}})$ and $w_{u,k}$ is the noise after the data accumulation.

Due to the co-location of the transmitter and the radar receiver, the transmit signal information can be shared. By performing a DFT on the u-th pulse of the transmit signal processing module, the following result can be obtained as

$$s_u(k) = \sum_{m=0}^{M-1} d_u(m) \mathrm{e}^{-\mathrm{j}2\pi k \frac{m}{M}}, \quad k = 0, \ldots, M-1. \tag{24}$$

Let $B_{u,k} = \tilde{b}_u(k)/s_u(k)$, and by representing $\{B_{u,k}\}$ of all accumulated pulse signals as a matrix, the observation matrix $\boldsymbol{B}$ can be derived as

$$\boldsymbol{B} = \begin{bmatrix} B_{0,0} & B_{0,1} & \cdots & B_{0,M-1} \\ B_{1,0} & B_{1,1} & \cdots & B_{1,M-1} \\ \vdots & \vdots & \ddots & \vdots \\ B_{U-1,0} & B_{U-1,1} & \cdots & B_{U-1,M-1} \end{bmatrix}. \tag{25}$$

Define $N_d = \lfloor R_{\max}/\Delta R \rfloor$ and $N_v = \lfloor \nu_{\max}/\Delta\nu \rfloor$ as the total number of possible distances and velocities of the target, respectively. We further define the delay transform matrix and the Doppler shift transform matrix as

$$\boldsymbol{F}_M \triangleq \mathrm{e}^{-\mathrm{j}2\pi \Delta f \boldsymbol{k}\boldsymbol{t}} \in \mathbb{C}^{M \times N_d}, \tag{26}$$

and

$$\boldsymbol{F}_U \triangleq \mathrm{e}^{\mathrm{j}2\pi T_{\text{PRI}} \boldsymbol{u}\boldsymbol{f}_d} \in \mathbb{C}^{U \times N_v}, \tag{27}$$

respectively, where $\boldsymbol{t} = [\tau_0, \ldots, \tau_{N_d-1}]$ is the target time delay vector, $\boldsymbol{f}_d = [f_0, \ldots, f_{N_v-1}]$ is the target Doppler vector, $\boldsymbol{k} \triangleq [0, \ldots, N-1]^{\mathrm{T}}$ is the time slot index vector and $\boldsymbol{u} \triangleq [0, \ldots, U-1]^{\mathrm{T}}$ is the pulse index vector. Therefore, the observation matrix $\boldsymbol{B}$ can be expressed as

$$\boldsymbol{B} = \boldsymbol{F}_U \boldsymbol{X} \boldsymbol{F}_M^{\mathrm{H}} + \tilde{\boldsymbol{W}}, \tag{28}$$

Algorithm 1 OMP algorithm for radar receiver.

Input: Matrix $\boldsymbol{\Phi}$, observation vector $\boldsymbol{b}$, target number L.
Output: Detected vector $\hat{\boldsymbol{x}}$.

$l = 1$, $\boldsymbol{r}_1 = \boldsymbol{b}$;
while $l \leqslant L$ **do**
  $i = \arg\max_i |\boldsymbol{\Phi}_i^{\mathrm{H}} \boldsymbol{r}_l|$;
  $S = S \cup \{i\}$;
  $\boldsymbol{P}_l = \boldsymbol{\Phi}_S(\boldsymbol{\Phi}_S^{\mathrm{H}}\boldsymbol{\Phi}_S)^{-1}\boldsymbol{\Phi}_S^{\mathrm{H}}$, $\boldsymbol{r}_{l+1} = (\boldsymbol{I} - \boldsymbol{P}_l)\boldsymbol{b}$;
  $l = l + 1$;
end while
$\hat{\boldsymbol{x}} = (\boldsymbol{\Phi}_S^{\mathrm{H}}\boldsymbol{\Phi}_S)^{-1}\boldsymbol{\Phi}_S^{\mathrm{H}}\boldsymbol{b}$;
Return $\hat{\boldsymbol{x}}$.

where $\boldsymbol{X} \in \mathbb{C}^{N_v \times N_d}$ represents the velocity-distance 2-dimensional image of the target, with non-zero values in the corresponding velocity and distance cells when there is a target or clutter. $\tilde{\boldsymbol{W}} \in \mathbb{C}^{U \times M}$ is composed of $\tilde{w}_{u,k} = w_{u,k}/b_u(k)$.

By leveraging the relationship between matrix multiplication and Kronecker product [19], we can reformulate (28) in vector form as

$$\mathrm{vec}(\boldsymbol{B}) = (\boldsymbol{F}_M \otimes \boldsymbol{F}_U)\,\mathrm{vec}(\boldsymbol{X}) + \mathrm{vec}(\tilde{\boldsymbol{W}}), \tag{29}$$

where $\mathrm{vec}(\cdot)$ denotes stacking the matrix by columns and the symbol $\otimes$ denotes the Kronecker product of the matrix. Defining $\boldsymbol{b} \triangleq \mathrm{vec}(\boldsymbol{B})$, $\boldsymbol{\Phi} \triangleq \boldsymbol{F}_M \otimes \boldsymbol{F}_U$, $\boldsymbol{x} \triangleq \mathrm{vec}(\boldsymbol{X})$ and $\tilde{\boldsymbol{w}} \triangleq \mathrm{vec}(\tilde{\boldsymbol{W}})$, then the above equation can be expressed as

$$\boldsymbol{b} = \boldsymbol{\Phi}\boldsymbol{x} + \tilde{\boldsymbol{w}}. \tag{30}$$

The algorithm for solving $\boldsymbol{x}$ can be described as

$$\hat{\boldsymbol{x}} = \arg\min_{\boldsymbol{x}} \|\boldsymbol{b} - \boldsymbol{\Phi}\boldsymbol{x}\|_2^2. \tag{31}$$

For CSC-IM, DFT-S-OFDM, and OFDM systems, the subcarriers either operate in the chirp domain or occupy all subcarriers in the frequency domain, making their processing steps similar to those of DFT-S-OFDM-IM. However, in the case of OFDM-IM, not all subcarriers in the frequency domain are occupied. This means that some subcarriers are invalid, resulting in a denominator of zero when directly dividing the received and transmitted frequency-domain signals. As a consequence, the elements of the observation matrix tend to approach infinity, rendering the algorithm ineffective. To overcome this challenge, we present a dedicated radar signal processing procedure tailored specifically for OFDM-IM.

Note that the OFDM-IM adopts the PIM mode. To uniformly represent the indices of active subcarriers, the modulation data of OFDM-IM symbols are serialized and transformed into a column, where the indices of active subcarriers can be arranged in ascending order, denoted by

$$\boldsymbol{I} = [i_1, i_2, \ldots, i_{\mathrm{GM}_s}]^{\mathrm{T}}. \tag{32}$$

Based on the index vector $\boldsymbol{I}$, the positions of the valid data in $\mathrm{vec}(\boldsymbol{B})$ can be determined. We define the selection matrix $\boldsymbol{Z} \in \mathbb{C}^{\mathrm{GM}_s \times \mathrm{GM}}$, whose matrix elements are

$$\boldsymbol{Z}_{z_x, z_y} = \begin{cases} 1, & i_{z_x} = z_y, \\ 0, & \text{otherwise}. \end{cases} \tag{33}$$

By left-multiplying both sides of (30) with matrix $\boldsymbol{Z}$, the selection process of active subcarrier data can be achieved. Let $\boldsymbol{b}_I = \boldsymbol{Z}\mathrm{vec}(\boldsymbol{B})$, $\boldsymbol{\Phi}_I = \boldsymbol{Z}(\boldsymbol{F}_M \otimes \boldsymbol{F}_U)$ and $\tilde{\boldsymbol{w}}_I = \boldsymbol{Z}\mathrm{vec}(\tilde{\boldsymbol{W}})$, then we have

$$\boldsymbol{b}_I = \boldsymbol{\Phi}_I\boldsymbol{x} + \tilde{\boldsymbol{w}}_I. \tag{34}$$

The algorithm for solving $\boldsymbol{x}$ in this case can be represented as

$$\hat{\boldsymbol{x}} = \arg\min_{\boldsymbol{x}} \|\boldsymbol{b}_I - \boldsymbol{\Phi}_I\boldsymbol{x}\|_2^2. \tag{35}$$

Orthogonal matching pursuit (OMP) is a classic algorithm in the field of compressive sensing and serves as the foundation for many widely-used algorithms. In this study, we employ OMP to solve (23)–(30) for parameter recovery, whose steps are outlined in Algorithm 1.

The computational burden primarily lies in the 3rd and 5th steps. In the 3rd step, where we have $\mathbf{\Phi} \in \mathbb{C}^{UM\times N_dN_v}$ and $\boldsymbol{r}_l \in \mathbb{C}^{UM\times 1}$, the matrix operation $\mathbf{\Phi}_i^{\mathrm{H}}\boldsymbol{r}_l$ has a complexity order of $\mathcal{O}(UMN_dN_v)$. Since it requires searching for the maximum value N_dN_v times, the complexity of the 1st step is $\mathcal{O}(UMN_d^2N_v^2)$. In the 5th step, where we have $\mathbf{\Phi}_S \in \mathbb{C}^{UM\times l}$, the complexity order can be approximated as $\mathcal{O}(U^2M^2)$. The OMP algorithm iterates for a total of L times. Therefore, the overall complexity of the algorithm is $\mathcal{O}(LUMN_d^2N_v^2 + LU^2M^2)$. Although the OMP algorithm has a relatively high complexity, it offers significant advantages such as high estimation accuracy and low hardware requirements that should not be overlooked.

5 Communication and radar signal processing for MIMO systems

In both communication and radar systems, MIMO not only enables higher data rates and more reliable communication but also enhances the radar system's ability to accurately estimate angles and improve measurement precision for various parameters.

In this section, we propose ISAC schemes that combine MIMO with the proposed DFT-S-OFDM-IM and other orthogonal waveforms. The model assumes the presence of uniform linear arrays at both the BS and user sides. The BS's array consists of a transmit antenna array and a radar receive antenna array, with N_t antennas serving as the dual-function transmit antennas and Q_r antennas for radar reception. At the user side, a communication receive antenna array with N_r antennas is utilized. The developed MIMO model enables the estimation of the target distance, velocity, and angle, making it suitable for applications involving multiple targets.

5.1 Communication receiver

In the context of DFT-S-OFDM-IM, taking into account the operation of multiple antennas, based on (8), the baseband signal transmitted by the n_t antennas can be described as

$$\begin{aligned} x_{n_t}(n) = &\sum_{k=0}^{MS-1}\sum_{m=0}^{M-1} d_{n_t}(m)\mathrm{e}^{-\frac{\mathrm{j}2\pi km}{M}}\mathrm{e}^{\frac{\mathrm{j}2\pi kn}{N}}, \\ &n = 0,1,\ldots,N-1. \end{aligned} \tag{36}$$

The frequency-domain expression of the transmitted signal from the n_t-th antenna can be obtained by applying the DFT to (36), given by

$$b_{n_t}(k) = \sum_{m=0}^{M-1} d_{n_t}(m)\mathrm{e}^{-\frac{\mathrm{j}2\pi km}{M}}, \quad k = 0,1,\ldots,M-1. \tag{37}$$

The transmit signal from the n_t-th antenna can be represented in vector form as $\boldsymbol{b}_{n_t} = [b_{n_t}(0),\ldots, b_{n_t}(M-1)]^{\mathrm{T}}$. At the communication receiver, the received signal at the n_r-th antenna is denoted by $\boldsymbol{y}_{n_r} = [y_{n_r}(0), y_{n_r}(1),\ldots, y_{n_r}(M-1)]^{\mathrm{T}}$. Then, we have

$$\boldsymbol{y}_{n_r} = \sum_{n_t=1}^{N_t} \boldsymbol{H}_{n_r,n_t}\boldsymbol{b}_{n_t} + \boldsymbol{w}_{n_r}, \quad n_r = 0,1,\ldots,N_r-1, \tag{38}$$

where $\boldsymbol{H}_{n_r,n_t}$ is the channel impulse response (CIR) matrix and its elements are assumed to follow a complex Gaussian distribution, $\boldsymbol{w}_{n_r} \in \mathbb{C}^{M\times 1}$ is the additive Gaussian white noise of the channel, which obeys a distribution of $\mathcal{CN}(0,\sigma^2)$, and σ^2 is the variance of the noise. The CIR matrix $\boldsymbol{H}_{n_r,n_t}$ is a circular matrix, and its first column is $\boldsymbol{h} = [h_1, h_2, \ldots, h_{\tilde{N}}, 0, \ldots, 0]^{\mathrm{T}}$, where $\tilde{N}$ is the number of multipath paths.

The frequency-domain response matrix of the channel and the received signal for each subcarrier can be denoted by $\tilde{\boldsymbol{H}}_k \in \mathbb{C}^{N_r\times N_t}$ and $\boldsymbol{y}(k) \in \mathbb{C}^{N_r\times 1}$, respectively, where $k = 0,1,\ldots,M-1$. The frequency-domain signal after MMSE equalization can be expressed as

$$\boldsymbol{r}(k) = \tilde{\boldsymbol{H}}_k^{\mathrm{H}}(\tilde{\boldsymbol{H}}_k\tilde{\boldsymbol{H}}_k^{\mathrm{H}} + \sigma^2\boldsymbol{I}_{N_r})^{-1}\boldsymbol{y}(k), \quad k = 0,1,\ldots,M-1. \tag{39}$$

We have $\boldsymbol{r}(k) = [r_1(k), \ldots, r_{n_t}(k), \ldots, r_{N_t}(k)] \in \mathbb{C}^{N_t \times 1}$, where $r_{n_t}(k)$ represents the received signal on the k-th subcarrier from the n_t-th transmit antenna. By performing an IDFT on $r_{n_t}(k)$ from each transmit antenna, we obtain

$$\tilde{d}_{n_t}(m) = \sum_{k=0}^{M-1} r_{n_t}(k) \mathrm{e}^{\frac{\mathrm{j}2\pi km}{M}}, \quad m = 0, 1, \ldots, M-1. \tag{40}$$

For the proposed MIMO-aided DFT-S-OFDM-IM system, similar to the SISO detection given by (16), the ML detection method for a given group can be formulated as

$$\left\{\hat{\boldsymbol{I}}_{n_t}, \hat{\boldsymbol{J}}_{n_t}\right\} = \arg \max_{i_{m_s}, j_{m_s}} \left\{\sum_{m_s=0}^{M_s-1} \tilde{d}_{n_t}(i_{m_s}) \mathrm{e}^{-\frac{\mathrm{j}2\pi j_{m_s}}{J}}\right\}, \tag{41}$$

where $\hat{\boldsymbol{I}}_{n_t}$ is the index vector of the active subcarriers and $\hat{\boldsymbol{J}}_{n_t}$ is the index vector of the PSK/QAM constellation points for the n_t-th transmit antenna. Based on (41), the estimation of the transmit signal in (36), namely $\hat{x}_{n_t}(n)$, is similar to the SISO case of (16).

Similar to SISO systems, the objective of radar signal processing in MIMO systems is to estimate three essential parameters, namely distance, velocity, and direction of multiple targets. These parameters correspond to the three primary dimensions of radar signals. Similar to SISO systems, these parameters of MIMO systems are also estimated through the utilization of an observation matrix.

In this subsection, we take the parameter estimation of multiple targets as an example. Suppose L point targets are located in the far field of the transmit antenna array. Their distances, velocities and angle parameters are r_l, v_l and θ_l, respectively, where $l \in \{0, 1, \ldots, L-1\}$. A schematic diagram of radar beam transmission is shown in Figure 3.

5.2 Radar sensing designs

The distance between the elements of the transmit uniform linear array is denoted by d_T, and the distance between the elements of the radar receive array is denoted by d_R. As shown in Figure 3, the transmit and receive arrays form a MIMO radar, i.e., $d_T = Q_r d_R$.

Let $n_t \in \{0, 1, \ldots, N_t - 1\}$ and $q_r \in \{0, 1, \ldots, Q_r - 1\}$ be the indices of the transmit and receive antennas, respectively. The signal on the m-th subcarrier received at the n_t-th antenna within the u-th pulse is given by

$$y_{u,q_r}^{(r)}(m, t) = \sum_{l=0}^{L-1} \alpha_l \sum_{n_t=0}^{N_t-1} x_{u,n_t}(m, t - \tau_{u,n_t,q_r}^l) + w_{u,q_r}^{(r)}(m, t), \tag{42}$$

where α_l is the reflection factor of the l-th target, τ_{u,n_t,q_r}^l is the round-trip delay between the n_t-th transmit antenna and the q_r-th receive antenna for the l-th target, $w_{u,q_r}^{(r)}(t)$ denotes the AWGN. When transmitting from the n_t-th antenna, the transmitted beam from this antenna serves as the reference beam. Assuming a uniform target motion within a CPI, the round-trip delay of the reference beam in Figure 3 can be expressed as $2(r_l + uv_l T_{\mathrm{PRI}})/c$.

Since the targets are in the far-field, for each antenna, both the departure angle of the ISAC array's transmitted beam and the arrival angle of the radar array's beam can be approximated as equal, as shown in the diagram, denoted by θ_l. Hence, the differences in travel distances caused by the positions of the transmit and receive antennas for estimating beams and reference beams are $n_t d_T \sin\theta_l$ and $q_r d_R \sin\theta_l$, respectively.

Therefore, the round-trip delay τ_{u,n_t,q_r}^l between the transmit antenna n_t and receive antenna q_r for the l-th target can be expressed as

$$\tau_{u,n_t,q_r}^l = \frac{2(r_l + uv_l T_{\mathrm{PRI}})}{c} - \frac{(n_t d_T + q_r d_R)\sin\theta_l}{c}. \tag{43}$$

In order to extract the useful information from the reflected echo, we perform separate calculations for each subcarrier. By synchronously mixing the received signal $y_{u,q_r}^{(r)}(m, t)$ with the transmitted waveform

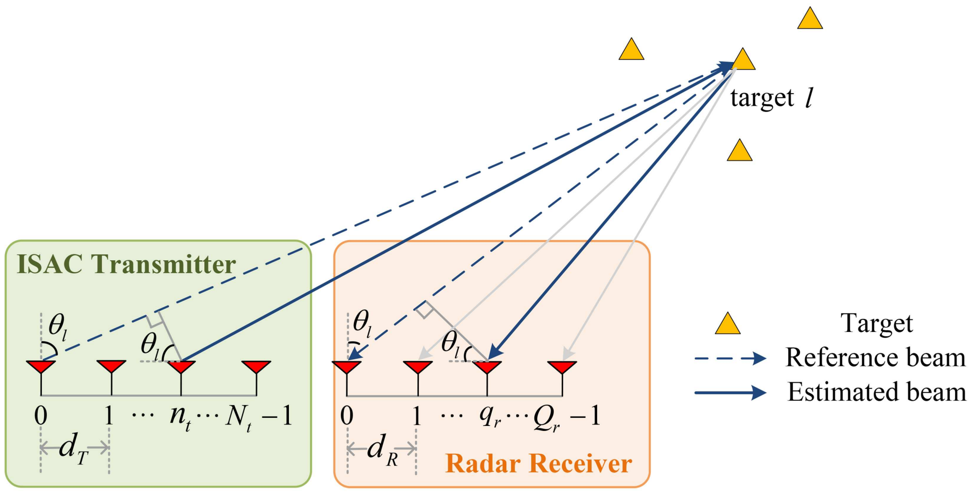

Figure 3 (Color online) ISAC-based MIMO radar system and beamforming diagram.

$x_{u,n_t}(m,t)$, we have

$$\begin{aligned} y^{(r)}_{u,n_t,q_r}(m,t) &= y^{(r)}_{u,q_r}(m,t)x^*_{u,n_t}(m,t) \\ &= \left\{ \sum_{l=0}^{L-1} \alpha_l \sum_{n_t=0}^{N_t-1} x_{u,n_t}(m, t-\tau^l_{u,n_t,q_r}) \right\} x^*_{u,n_t}(m,t) + \tilde{w}^{(r)}_{u,q_r}(m,t). \end{aligned} \tag{44}$$

The obtained signal $y^{(r)}_{u,n_t,q_r}(m,t)$ is fed into a low-pass filter (LPF), and each pulse retains a single data sampling point. Therefore, the separated signal received by the q_r-th receiving antenna is given by

$$y^{(r)}_{u,n_t,q_r}(m) = \sum_{l=0}^{L-1} \alpha_l \left\{ \sum_{\tilde{n}_t=0}^{N_t-1} d_{\tilde{n}_t}(m) \right\} d^*_{n_t}(m) \mathrm{e}^{-\mathrm{j}2\pi f_m \tau^l_{u,n_t,q_r}} + \tilde{w}^{(r)}_{u,n_t,q_r}(m), \tag{45}$$

where $f_m = f_c + mB_{\text{sub}}$ represents the modulation frequency of the m-th subcarrier, B_{sub} is the subcarrier spacing and $\tilde{w}^{(r)}_{u,k,q_r}(t)$ is a band-limited AWGN. Substituting the expression of τ^l_{u,n_t,q_r} in (43) into (45), we obtain

$$y^{(r)}_{u,n_t,q_r}(m) = \sum_{l=0}^{L-1} \eta_l(m) \mathrm{e}^{-\mathrm{j}2\pi\left[m\tilde{f}^l_r + \tilde{\delta}_{u,k}(m)\tilde{f}^l_v u + \delta_{u,k}\tilde{f}^l_\theta (Q_r n_t + q_r)\right]} + \tilde{w}^{(r)}_{u,n_t,q_r}(m), \tag{46}$$

where $\tilde{\delta}_{u,k}(m) = f_m/f_c$ represents the relative factor of carrier frequency, $\tilde{f}^l_r = \frac{2r_l B_{\text{sub}}}{c}$ is the normalized frequency related to distance parameters, $\tilde{f}^l_v = \frac{2v_l T_{\text{PRI}} f_c}{c}$ is the normalized frequency related to velocity parameters, and $\tilde{f}^l_\theta = \frac{d_R \sin\theta_l f_c}{c}$ is the normalized frequency related to spatial parameters. These three terms respectively contain the information relating to the target range, velocity, and angle that we are interested in. By estimating the values of f^l_r, f^l_v, and f^l_θ, the target parameters can be obtained. Moreover, $\eta_l(m)$ in (46) is given by

$$\eta_l(m) = \alpha_l d^*_{n_t}(m) \mathrm{e}^{-\frac{\mathrm{j}4\pi r_l f_c}{c}} \sum_{\tilde{n}_t=0}^{N_t-1} d_{\tilde{n}_t}(m). \tag{47}$$

We construct the perceptual observation matrix $\boldsymbol{A} \in \mathbb{C}^{N_t Q_r UM \times UMQ}$, where $Q = N_t Q_r$. Defining variables $\tilde{\varsigma} = n_t Q_r UM + q_r UM + uM + m$ and $\tilde{\xi} = \tilde{u}MQ + \tilde{m}Q + q$, where $\tilde{u} \in \{0, 1, \ldots, U-1\}$, the elements of row $\tilde{\varsigma}$ and column $\tilde{\xi}$ of matrix $\boldsymbol{A}$ are given as follows:

$$[\boldsymbol{A}]_{\tilde{\varsigma},\xi} = \mathrm{e}^{-\mathrm{j}2\pi\left[\frac{m\tilde{m}}{M} + \tilde{\delta}_{u,k}(m)u(\frac{\tilde{u}}{U} - \frac{1}{2}) + \tilde{\delta}_{u,k}(m)(Q_r n_t + q_r)\frac{q}{Q}\right]}. \tag{48}$$

In order to represent the radar target recovery as a sparse recovery problem, signal $y^{(r)}_{u,n_t,q_r}(m)$ in (44) is organized in vector form $\boldsymbol{y}^{(r)}$, which represents the useful information received by the radar during a

Table 1 System parameters and explanations.

Notation	Value	Parameter
f_c	2 GHz	Carrier frequency
N_{syms}	1024	Number of OFDM symbols
Δf	400 kHz	Subcarrier spacing
F_s	51.2 MHz	Sampling frequency
M	128	Number of subcarriers/slots
T_{PRI}	0.5 ms	Pulse interval

CPI. Each element of the vector is denoted by $[\boldsymbol{y}]_{\varsigma}^{(r)} = y_{u,n_t,q_r}^{(r)}(m)$. The relationship between vector $\boldsymbol{y}^{(r)}$ and observation matrix $\boldsymbol{A}$ is

$$\boldsymbol{y}^{(r)} = \boldsymbol{A}\boldsymbol{b} + \boldsymbol{w}^{(r)}, \tag{49}$$

where $\boldsymbol{b}$ is a sparse vector with the size of $UMQ \times 1$ and its sparsity level is the number of the targets L.

The elements of $\boldsymbol{b}$ are represented as

$$\boldsymbol{b}_{\xi} = \begin{cases} \eta_l(m), & (f_r^l, f_v^l, f_\theta^l) = (m/M, u/U - 1/2, q/Q), \\ 0, & \text{otherwise.} \end{cases} \tag{50}$$

Therefore, the target parameters can be obtained by determining the positions of the non-zero values. Solving $\boldsymbol{b}$ is equivalent to solving the following:

$$\hat{\boldsymbol{b}} = \arg\min_{\boldsymbol{b}} \left\| \boldsymbol{y}^{(r)} - \boldsymbol{A}\boldsymbol{b} \right\|_2^2. \tag{51}$$

Since the number of rows in $\boldsymbol{A}$ is generally smaller than the number of columns, the values of $\boldsymbol{b}$ are not unique. However, by imposing the condition of sparsity, the solution can be obtained using compressive sensing based reconstruction algorithms. If $\boldsymbol{b}_{\xi}$ is solved and found to be non-zero, the corresponding target's distance, velocity, and angle can be calculated based on the conditions of non-zero values and the definitions of f_r^l, f_v^l, and f_θ^l in (46) as follows:

$$\hat{r} = \frac{cm}{2B_{\text{sub}}M}, \tag{52}$$

$$\hat{v} = \frac{c}{2T_0 f_c (u/U - 1/2)}, \tag{53}$$

and

$$\hat{\theta} = \arcsin\left\{ \frac{cq}{f_c d_R Q} \right\}, \tag{54}$$

respectively.

6 Comparative performance analysis

In this section, we present the simulation results and performance comparisons of ISAC systems using the proposed DFT-S-OFDM-IM and other classic orthogonal waveforms as demonstrated in Section 2. We compare different waveforms under fair parameter settings with the same transmission rates. The main simulation settings are shown in Table 1. In our simulation, the Doppler frequency shift is based on the scenario of vehicle networking and is randomly generated. For detection, the ML-based detectors given in (16) and (41) are adopted for SISO and MIMO systems, respectively.

6.1 Peak-to-average power ratio

In this subsection, we compare the PAPR characteristics of waveforms with different numbers of indices, and give simulation results for the NPIM and PIM cases separately.

Figure 4 compares the complementary cumulative distribution functions (CCDFs) of the PAPRs of OFDM-IM, CSC-IM and DFT-S-OFDM-IM in the NPIM mode. Since the available bandwidths for OFDM-IM and DFT-S-OFDM-IM are $M \times \Delta f$, and for CSC-IM is $D \times \Delta f$, the bandwidth for CSC-IM

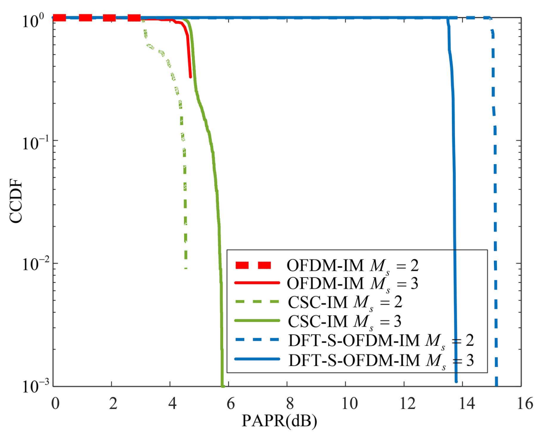

Figure 4 (Color online) PAPR comparison of OFDM-IM, CSC-IM, and the proposed DFT-S-OFDM-IM under the NPIM mode.

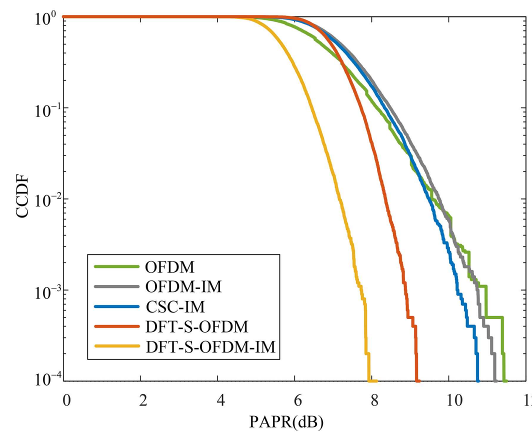

Figure 5 (Color online) PAPR comparison of OFDM-IM, CSC-IM, and DFT-S-OFDM-IM under the PIM mode.

waveform is set as $D = M = 128$ for the purpose of fair comparison. Due to the exponential growth in computational complexity with increasing subcarriers, NPIM can only activate a limited number of subcarriers. We consider $M_s = 2$ and $M_s = 3$, both utilizing QPSK modulation. It can be observed that OFDM-IM has the lowest PAPR, CSC-IM is slightly worse, while DFT-S-OFDM-IM has a higher PAPR. This means that the PAPR performance of DFT-S-OFDM-IM is worse in the NPIM case. It is worth noting that while the PAPRs of OFDM-IM and CSC-IM waveforms increase with the number of activated indices M_s, the PAPR of DFT-S-OFDM-IM waveform decreases as M_s increases.

The communication system can achieve a higher transmission rate when the PIM mode is used. We choose OFDM, OFDM-IM, DFT-S-OFDM, CSC-IM, and DFT-S-OFDM-IM with the number of subcarriers/time slots set to $M = 128$. BPSK modulation is used for both OFDM and DFT-S-OFDM. For OFDM-IM, CSC-IM and DFT-S-OFDM-IM, the subcarriers/time slots are divided into $G = 32$ groups with 4 subcarriers/time slots in each group, in which the active subchirps are modulated in QPSK. One subcarrier/time slot is selected for activation in each group. The transmission rate of 128 bits/symbol is guaranteed for all the comparison systems. Figure 5 plots the PAPR of five different waveforms in the PIM case. From Figure 5, it can be observed that the PAPRs of these five waveforms in descending order are OFDM, OFDM-IM, CSC-IM, DFT-S-OFDM, and DFT-S-OFDM-IM. Unlike the NPIM mode, OFDM-IM and CSC-IM have lost the PAPR advantage, when the proposed DFT-S-OFDM-IM has the lowest PAPR. At a CCDF of 10^{-4}, the PAPR of DFT-S-OFDM-IM is about 1 dB lower than that of DFT-S-OFDM and more than 3 dB lower than that of OFDM.

6.2 Bit error rate

We employ the extended vehicular a model (EVA) multipath fading channel as the communication channel, and other parameters are shown in Table 1. For the NPIM case, Figure 6 compares the BERs of OFDM-IM, CSC-IM, and the proposed DFT-S-OFDM-IM. Based on (10), the cases with no index interval $\Delta = 1$ (denoted by NIS) and with an index interval of $\Delta = 20$ (denoted by IS) are considered, and the number of index modulation activated subcarriers/slots is $M_s = 2$. As shown in Figure 6, the BER performance of the proposed DFT-S-OFDM-IM is the best, followed by CSC-IM and OFDM-IM. Therefore, although the PAPR of DFT-S-OFDM-IM in the NPIM mode is higher, it still has a hard-to-ignore advantage in transmission accuracy. It is worth noting that regardless of the method used, increasing the subcarrier spacing helps reduce the BER. However, the setting of the subcarrier spacing reduces the number of optional index combinations, which leads to a decrease in transmission rate. Therefore, this BER reduction comes at the expense of the transmission rate.

Figure 7 illustrates the BERs of OFDM, OFDM-IM, DFT-OFDM, CSC-IM, and DFT-OFDM-IM in the PIM case. For the OFDM-IM waveform, we consider the interleaved subcarrier index modulation (ISIM) and subcarrier index modulation (SIM). It can be seen that the BER improvement of OFDM-SIM is not significant compared to OFDM. However, the BER performance of OFDM-ISIM has surpassed that of OFDM at high SNRs, while the DFT-S-OFDM-IM waveform still has the best BER performance.

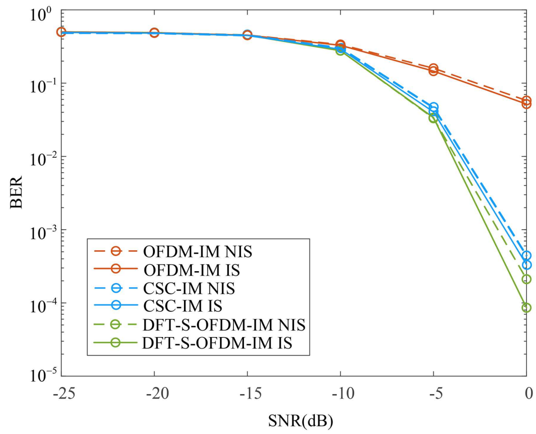

Figure 6 (Color online) BER performance comparison of OFDM-IM, CSC-IM, and the proposed DFT-S-OFDM-IM under the NPIM mode.

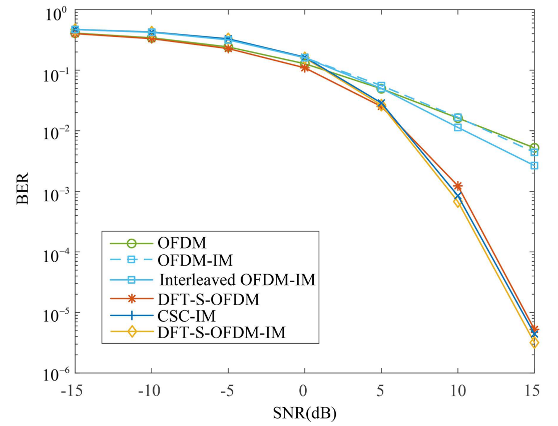

Figure 7 (Color online) BER performance comparison of OFDM, OFDM-IM, DFT-S-OFDM, CSC-IM, and the proposed DFT-S-OFDM-IM under the PIM mode.

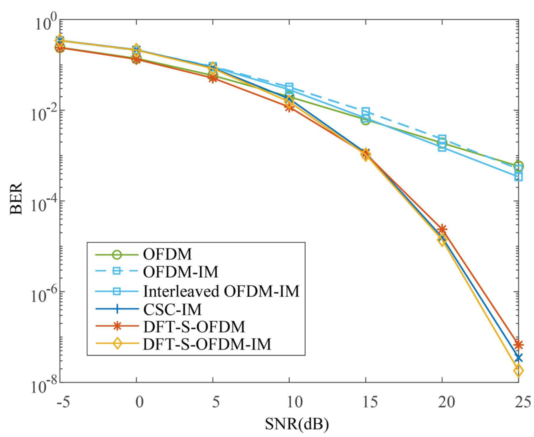

Figure 8 (Color online) BER performance comparison in MIMO systems with OFDM, OFDM-IM, DFT-S-OFDM, CSC-IM, and the proposed DFT-S-OFDM-IM waveforms.

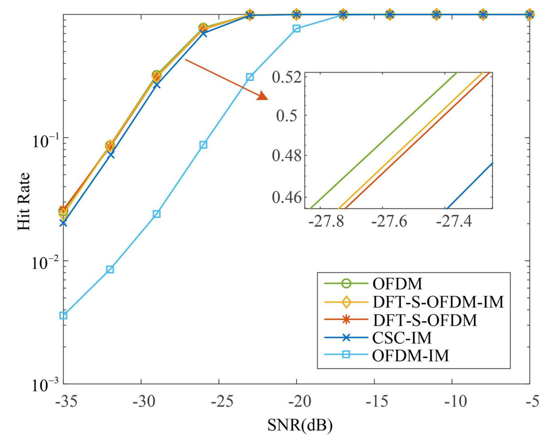

Figure 9 (Color online) Hit rate performance comparison in SISO systems with OFDM, OFDM-IM, DFT-S-OFDM, CSC-IM, and DFT-S-OFDM-IM waveforms.

Therefore, whether in NPIM or PIM scenarios, DFT-S-OFDM-IM demonstrates its significant advantages.

In the MIMO system simulation, setting $N_t = N_r = 4$ and other parameter settings are consistent with the single-antenna simulation, the BERs of the five waveforms are obtained as shown in Figure 8. The BER performance of DFT-S-OFDM-IM remains the best, followed by that of CSC-IM. It can be seen that DFT precoding improves the BER performance significantly, and at BER $= 10^{-3}$, the DFT precoded waveform has an SNR gain about 10 dB compared to conventional waveforms. The BER performance of OFDM-IM is better than that of OFDM at high SNRs, and DFT-S-OFDM-IM also further improves the performance of DFT-S-OFDM, thanks to the advantage of IM.

6.3 Hit rate

To demonstrate the performance of the radar under different noise levels, we employed hit rate as the performance evaluation metric for radar perception. A "successful hit" occurs if the range-velocity-angle parameter of a scattering point is successfully recovered. It is noted that hit rate is a good performance metric for target tracking in the Internet of Vehicles. Each hit rate is calculated over 20000 Monte Carlo trials by recovering the target scenario depicted in Figure 3.

The resolution and estimation range of the target parameters are fixed once the waveform parameters and transmit-receive array configuration are determined. This allows for the derivation of all possible target parameter combinations, which is a finite number. The hit rate is then calculated by comparing the number of successful hits to the total number of target parameter combinations.

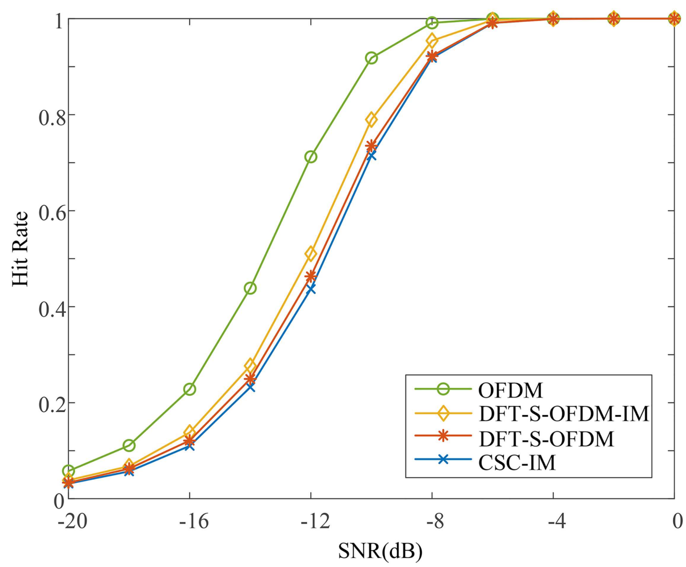

Figure 10 (Color online) Hit rate performance comparison in MIMO systems with OFDM, DFT-S-OFDM, CSC-IM, and the proposed DFT-S-OFDM-IM waveforms.

Figure 9 illustrates the radar performance of the five dual-function waveforms under PIM mode. OFDM-IM has the worst performance and a significant gap compared to the other OFDM variants due to the fact that the OFDM-IM signal does not utilize all the frequency domain subcarriers. The other waveforms utilize information from all subcarriers due to the time slot IM. The hit rate differences among the other four waveforms are relatively small, ranked from highest to lowest as OFDM, DFT-S-OFDM-IM, DFT-S-OFDM, and CSC-IM. OFDM performs the best among the five waveforms due to its lower "frequency-domain signal randomness" compared to the DFT pre-coded waveform. Specifically, DFT-S-OFDM, due to its unique DFT precoding step, can indeed generate a smoother and more uniform frequency domain amplitude distribution, which can be understood as a form of "high randomness" because it reduces the peak power of specific frequency components, making the signal appear more random and flat. Relatively speaking, OFDM may exhibit more peaks and valleys due to direct modulation on each subcarrier, and therefore may be considered as "low randomness". As a result, it is less susceptible to the interference caused by the randomness of symbols during target parameter detection.

Due to the poor perceptual performance of the OFDM-IM waveform compared to other waveforms, we only compare the other four waveforms in the MIMO radar performance simulation, as shown in Figure 10. We perform 20000 Monte Carlo experiments with $M = 16$. The results indicate that while there are variations in the target hit rates across different waveforms in the MIMO system, and these variations do not impact on the waveform perceptual performance. As shown in Figure 10, the proposed DFT-S-OFDM-IM demonstrates attractive radar performance among the considered waveforms. In summary, while OFDM excels in radar functionality, it lags in communication performance. Conversely, the DFT-S-OFDM-IM waveform, though marginally below OFDM in radar noise resilience, significantly outperforms OFDM in communication capabilities, rendering it an optimum candidate for ISAC applications as an ideal dual-functional waveform. Furthermore, it is evident that the unified ISAC framework proposed herein seamlessly accommodates OFDM and its variant waveforms, thereby facilitating adaptable system designs and enhancing operational flexibility.

7 Conclusion

In this paper, we proposed a concise and unified system framework that facilitated the application of orthogonal linear phase subcarrier waveforms, namely OFDM and its variant waveforms, in ISAC systems. This pioneering work introduced the innovative DFT-S-OFDM-IM waveform and devised signal processing techniques tailored to both SISO and MIMO architectures in an integrated fashion. Extensive performance evaluations were conducted from multifaceted viewpoints, examining PAPR fluctuations under dual indexing scenarios and comparing the BERs of various waveforms in fading channels to assess their communication efficacy. Radar performance was scrutinized through the investigation of detection hit rates. The simulation results resoundingly validated the superiority of the proposed DFT-S-OFDM-IM, which not only excelled in reducing the PAPR and BER compared to alternative waveforms but also attained attractive radar detection capabilities, thereby affirming its effectiveness as a promising solution for ISAC systems.

Acknowledgements This work was supported by National Key R&D Program of China (Grant No. 2023YFE0115100), Sichuan Science and Technology Program (Grant No. 2024YFHZ0051), Fundamental Research Funds for the Central Universities (Grant No. 2242022k60006), and Meituan Academy of Robotics Shenzhen (Grant No. 231565).

References

1 Kaushik A, Singh R, Dayarathna S, et al. Toward integrated sensing and communications for 6G: key enabling technologies, standardization, and challenges. IEEE Comm Stand Mag, 2024, 8: 52–59
2 Yang P, Xiao Y, Xiao M, et al. 6G wireless communications: vision and potential techniques. IEEE Netw, 2019, 33: 70–75
3 Alwis C D, Kalla A, Pham Q V, et al. Survey on 6G frontiers: trends, applications, requirements, technologies and future research. IEEE Open J Commun Soc, 2021, 2: 836–886
4 Zhang Z, Xiao Y, Ma Z, et al. 6G wireless networks: vision, requirements, architecture, and key technologies. IEEE Veh Technol Mag, 2019, 14: 28–41
5 Zhang J A, Rahman M L, Wu K, et al. Enabling joint communication and radar sensing in mobile networks — a survey. IEEE Commun Surv Tut, 2022, 24: 306–345
6 Zhu G X, Lyu Z H, Jiao X, et al. Pushing AI to wireless network edge: an overview on integrated sensing, communication, and computation towards 6G. Sci China Inf Sci, 2023, 66: 130301
7 Levanon N. Multifrequency radar signals. In: Proceeding of IEEE International Radar Conference, Alexandria, 2000. 683–688
8 Sturm C, Zwick T, Wiesbeck W. An OFDM system concept for joint radar and communications operations. In: Proceeding of the 69th Vehicular Technology Conference, Barcelona, 2009. 1–5
9 Surender S C, Narayanan R M. UWB noise-OFDM netted radar: physical layer design and analysis. IEEE Trans Aerosp Electron Syst, 2011, 47: 1380–1400
10 Schindler D, Schweizer B, Knill C, et al. MIMO-OFDM radar using a linear frequency modulated carrier to reduce sampling requirements. IEEE Trans Microwave Theor Techn, 2018, 66: 3511–3520
11 Wang Y, Cao Y, Yeo T S, et al. Joint sequence optimization-based OFDM waveform design for integrated radar and communication systems. IEEE Trans Veh Technol, 2022, 71: 12734–12748
12 Zhou Z C, Liu B, Shen B S, et al. Doppler-resilient waveform design in integrated MIMO radar-communication systems. Sci China Inf Sci, 2024, 67: 112301
13 Wang J, Varshney N, Gentile C, et al. Integrated sensing and communication: enabling techniques, applications, tools and data sets, standardization, and future directions. IEEE Int Things J, 2022, 9: 23416–23440
14 Wei Z, Yuan W, Li S, et al. Orthogonal time-frequency space modulation: a promising next-generation waveform. IEEE Wireless Commun, 2021, 28: 136–144
15 Bemani A, Ksairi N, Kountouris M. Affine frequency division multiplexing for next generation wireless communications. IEEE Trans Wireless Commun, 2023, 22: 8214–8229
16 Chen X, Cui J, Ni W, et al. DFT-S-OFDM: enabling flexibility in frequency selectivity and multiuser diversity for 5G. IEEE Consumer Electron Mag, 2020, 9: 15–22
17 Mietzner J. DFT-spread OFDM MIMO-radar — an alternative for reduced crest factors. In: Proceeding of the 20th International Radar Symposium (IRS), Ulm, 2019. 1–10
18 Zhu X, Yuan L, Li Q, et al. On the performance of 3-D spatial modulation over measured indoor channels. IEEE Trans Veh Technol, 2022, 71: 2110–2115
19 Cheng X, Zhang M, Wen M, et al. Index modulation for 5G: striving to do more with less. IEEE Wireless Commun, 2018, 25: 126–132
20 Mao T, Wang Q, Wang Z, et al. Novel index modulation techniques: a survey. IEEE Commun Surv Tut, 2019, 21: 315–348
21 Chen H, Xiao Y, Fang S, et al. Low-complexity transmit antenna selection for offset spatial modulation. Sci China Inf Sci, 2022, 65: 192302
22 Uthayakumar T, Mei J, Wang X. Multi-dimensional modulation for data rate maximization in non-orthogonal spatial-time-frequency domains. In: Proceeding of the 4th 5G World Forum (5GWF), Montreal, 2021. 76–81
23 Zhang K, Hai H, Wen M, et al. Generalized space-code index modulation for high rate and energy-efficient MIMO transmission. IEEE Trans Veh Technol, 2021, 70: 12812–12820
24 Şahin A, Hoque S S M, Chen C Y. Index modulation with circularly-shifted chirps for dual-function radar and communications. IEEE Trans Wireless Commun, 2022, 21: 2938–2952
25 Zhao J R, Yang P, Xiao Y, et al. A new FMCW-based multi-domain joint modulation dual-function radar communication technology (in Chinses). Sci Sin Inform, 2023, 53: 1802–1821
26 Şahin M M, Gurol I E, Arslan E, et al. OFDM-IM for joint communication and radar-sensing: a promising waveform for dual functionality. Front Comms Net, 2021, 2: 715944
27 Cao A, Xiao L, Xiao P, et al. A tight upper bound for enhanced DCT-OFDM with index modulation. IEEE Trans Veh Technol, 2020, 69: 16213–16217
28 He C, Cao A, Xiao L, et al. Enhanced DCT-OFDM system with index modulation. IEEE Trans Veh Technol, 2019, 68: 5134–5138
29 Şahin A, Hosseini N, Jamal H, et al. DFT-spread-OFDM-based chirp transmission. IEEE Commun Lett, 2021, 25: 902–906